

Mechanotransduction and flow across the endothelial glycocalyx

Sheldon Weinbaum*[†], Xiaobing Zhang*, Yuefeng Han*, Hans Vink[‡], and Stephen C. Cowin*

*Departments of Biomedical and Mechanical Engineering, City College of the City University of New York, New York, NY 10031; and [‡]Department of Medical Physics, Academic Medical Center, University of Amsterdam, P.O. Box 22700, 1100 DE Amsterdam, The Netherlands

This contribution is part of the special series of Inaugural Articles by members of the National Academy of Sciences elected on April 30, 2002.

Contributed by Sheldon Weinbaum, May 9, 2003

In this inaugural paper, we shall provide an overview of the endothelial surface layer or glycocalyx in several roles: as a transport barrier, as a porous hydrodynamic interface in the motion of red and white cells in microvessels, and as a mechanotransducer of fluid shearing stresses to the actin cortical cytoskeleton of the endothelial cell. These functions will be examined from a new perspective, the quasiperiodic ultrastructural model proposed in Squire *et al.* [Squire, J. M., Chew, M., Nneji, G., Neal, C., Barry, J. & Michel, C. (2001) *J. Struct. Biol.* 136, 239–255] for the 3D organization of the endothelial surface layer and its linkage to the submembranous scaffold. We shall show that the core proteins in the bush-like structures comprising the matrix have a flexural rigidity, EI , that is sufficiently stiff to serve as a molecular filter for plasma proteins and as an exquisitely designed transducer of fluid shearing stresses. However, EI is inadequate to prevent the buckling of these protein structures during the intermittent motion of red cells or the penetration of white cell microvilli. In these cellular interactions, the viscous draining resistance of the matrix is essential for preventing adhesive molecular interactions between proteins in the endothelial membrane and circulating cellular components.

Although the endothelial surface glycocalyx was first identified by special electron microscopic staining techniques nearly 40 years ago (1), it is only relatively recently that this surface layer has been observed *in vivo* (2) and the importance of its multifaceted physiological functions recognized. Key among these functions are its role as a molecular sieve in determining the oncotic forces that are established across microvessel endothelium (3–6), its role as a hydrodynamic exclusion layer preventing the interaction of proteins in the red cell and endothelial cell membranes (7–9), its function in modulating leukocyte attachment and rolling (10) and as a transducer of mechanical forces to the intracellular cytoskeleton in the initiation of intracellular signaling, as proposed herein.

It is widely recognized that fluid shearing forces acting on endothelial cells (ECs) have a profound effect on EC morphology, structure, and function (11, 12). It is now also clear from theoretical considerations (7, 9, 13, 14) that the shear stress at the edge of the endothelial surface layer is greatly attenuated by the extracellular matrix of proteoglycans and glycoproteins in the glycocalyx, with the result that fluid velocities, except near the edge of the layer, are vanishingly small. Thus, the shear stress due to the fluid flow acting on the apical membrane of the EC itself is negligible. This paradoxical prediction has raised a fundamental question as to how hydrodynamic and mechanical forces, more generally, are transmitted across the structural components of the glycocalyx. How do these components deform under the action of these forces, and how are these forces and deformations communicated to the underlying cortical cytoskeleton (CC)?

Little was known about the specific proteins or generalized structure of the glycocalyx until recently (15–17). The state of knowledge before 2000 is summarized in ref. 18. *In vivo* experiments demonstrated that hyaluronan and chondroitin sulfate play an important role in the assembly of the layer and its sieving properties (17). Using computed autocorrelation functions and Fourier trans-

forms of electron microscopic images obtained from both new (15) and previous (19) studies of frog mesenteric capillaries, Squire *et al.* (15) were able to identify for the first time the quasiperiodic substructure of the glycocalyx and the anchoring foci that appear to emanate from the underlying CC. The computer-enhanced images showed that the glycocalyx is a 3D fibrous meshwork with a characteristic spacing of 20 nm in all directions and that the effective diameter of the periodic scattering centers was 10–12 nm. Using a freeze-fracture replica from a rare section where the fracture plane passed parallel and close to the endothelial surface, they also showed that anchoring foci formed a hexagonal array with an intercluster spacing of typically 100 nm in frog lung capillary. This latter observation was consistent with the spacing of bush-like structures seen on the plasmalemma of the fenestrated renal capillaries of the rat by using a new fluorocarbon oxygen fixation technique, which preserved the portion of the glycocalyx close to the EC surface (20).

On the basis of the foregoing observations, Squire *et al.* (15) proposed a model for the structural organization of the endothelial surface layer (ESL) and its relationship to the EC CC. The model provides a new view of the organization of the matrix that forms the molecular sieve for the filtering of plasma proteins. The possible existence of an ordered structure was first proposed by Michel (21) to explain why there is a sharp break in the solute permeability curve for molecules the size of albumin. These ideas will be used in the present paper to formulate a mathematical model for analyzing the transduction of mechanical forces and bending moment across the ESL. We first address a basic question: What is the bending rigidity EI of the core proteins comprising the glycocalyx that enables them to resist the randomizing forces of Brownian motion and deformation by fluid shear stresses? To answer this question, we shall examine the time-dependent recovery of the surface layer after it has been crushed by the passage of a white blood cell (WBC).[§] Theoretical models are then developed to explore the deformability of the matrix in both red and white cell interactions and in response to fluid shearing forces. The forces and torques exerted on the structural elements of the ESL by these mechanical loads are then used to predict the stresses transmitted to the CC.

A unique feature of the present analysis is the attempt to couple the dynamic response of the surface layer to mechanical loading to the stresses and deformations induced in the underlying CC. This CC has previously been explored in other contexts involving the movement of plasma proteins in the plane of the membrane using single-particle tracking and optical traps (23, 24). These studies, summarized in ref. 24, have led to a “fence” model construct in which one observes microdomains as small as

Abbreviations: EC, endothelial cell; CC, cortical cytoskeleton; ESL, endothelial surface layer; WBC, white blood cell; TJ, tight junction; GAG, glycosaminoglycans.

[†]To whom correspondence should be addressed at: Departments of Biomedical and Mechanical Engineering, City College of New York of the City University of New York, 138th Street at Convent Avenue, New York, NY 10031. E-mail: weinbaum@ccny.cuny.edu.

[§]Vink, H., Duling, B. R. & Spaan, J. A. E. (1999) *FASEB J.* 13, A11 (abstr.).

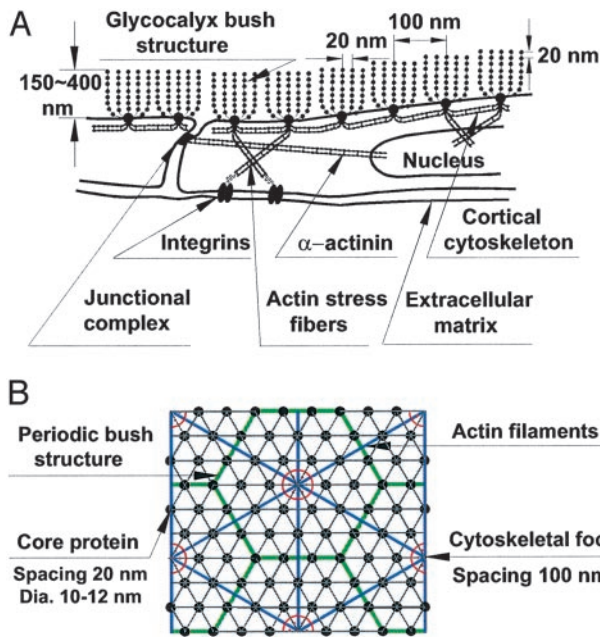


Fig. 1. (A) Sketch of ESL (not to scale) showing core protein arrangement and spacing of scattering centers along core proteins and their relationship to actin CC as proposed in ref. 15. (B) *En face* view of idealized model for core protein clusters and cluster foci and their relationship to hexagonal actin lattice in CC.

0.01 mm² restricting the movement of proteins due to the interaction of their cytoplasmic tails with the underlying cytoskeletal scaffold.

Structural Model. Fig. 1A is a modified sketch of the structural model proposed in ref. 15 for the organization of the core proteins in the proteoglycan clusters that comprise the glycocalyx and their linkage to the underlying CC. This composite structure is deduced from the appearance of bush-like structures that appear to emanate from foci in the cell membrane (20) and current models of the CC (24). Also shown are transcellular actin stress fibers linked by α-actinin tethering the cortical shell to focal adhesion sites of integrins on the basal aspect of the cell and other tethering filaments associated with actin filament bundles in close proximity to the junctional complexes (11, 12). There is a bidirectional grid with 20-nm periodicity of scattering centers aligned along the axes of the core proteins. There is also a 100-nm periodicity associated with the separation of each cluster and the observed hexagonal organization of the membrane bound foci. Fig. 1B is an *en face* view of our idealized model that assumes both a hexagonal arrangement of the core proteins in each cluster and a hexagonal arrangement of the actin filaments in the underlying CC. We assume that each of the membrane foci is connected by short linker molecules at the intersections of the hexagonal actin lattice that forms the cortical network. On the basis of the length of the cytoplasmic tails and the typical forces exerted by optical tweezers in dragging membrane proteins across domain boundaries, these linkages are both short and relatively rigid (24).

Transport Model. We first consider the transport aspects of the new structural model for the ESL. In earlier studies (25), the authors assumed a model for transport across microvessel endothelium that involved a single nearly continuous tight junction (TJ) strand with periodic discontinuities of length $2d$ and spacing $2D$ in series with surface glycocalyx that permitted the passage of water and small solutes but greatly restricted the passage of

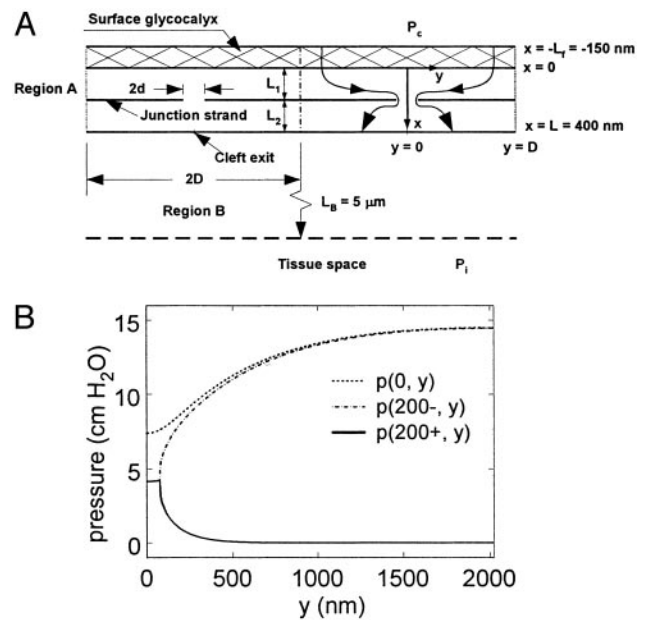


Fig. 2. (A) Model geometry taken from ref. 5. (B) Pressure distribution behind ESL and fore and aft of TJ strand in mathematical model for flow through cleft of frog mesentery capillary.

plasma proteins, in particular albumin (7-nm diameter, Fig. 24). The dimensions in this diagram correspond to the detailed measurements of the TJ ultrastructure in frog mesentery capillary (26). In the past, the molecular sieve associated with the ESL was assumed to be a fiber matrix composed of glycoproteins with extended glycan (GAG) side chains of typically 0.6-nm radius and 7- to 8-nm gap spacing associated with the disaccharide repeat along the core protein. This repeat distance was assumed in ref. 25 and subsequent studies by the authors (5, 6) to provide the dimensions of the molecular sieve for albumin. It is typical of the 2D appearance of GAG side chains along chondroitin sulfate proteoglycans when observed on carbon filters (27).

The foregoing model for the sieving structure of the glycocalyx led Michel (3) and Weinbaum (4) to propose that Starling forces should be applied locally across just the endothelial glycocalyx rather than across the entire endothelial layer between plasma and tissue, as had been universally done in the past. This new hypothesis is quantitatively examined in ref. 5, where it is shown that the converging flow through the orifice-like breaks in the TJ strand will prevent back diffusion from the tissue space with the result that the protein concentration in the tissue can differ greatly from that behind the glycocalyx layer when the Peclet number at the breaks is >1 . Strong evidence in support of this hypothesis is provided by the theory and experiments in ref. 6, in which the tissue is backloaded so there is no effective oncotic pressure difference between plasma and tissue. The experiments clearly demonstrate that at high flow rates, the proteins on the lumen side of the TJ strand are washed out, and nearly the full oncotic pressure is felt across the ESL although the tissue oncotic pressure is isotonic with respect to plasma.

The model proposed in ref. 15 provides an alternative picture for the sieving structure. Proteoglycans with extended GAG side chains are replaced by fibers with periodic molecular structures of 10- to 12-nm diameter distributed at 20-nm intervals along the core protein. These particles could either be aggregated GAGs that take on a spherical appearance or plasma proteins that are attracted by negative charge repeats. Squire *et al.* (15) show that for an ordered square lattice, the fractional area of the pores available for the transport of albumin is reduced to nearly zero

when the effective fiber radius of the core protein is 6 nm, the observed radius of the scattering centers. According to fiber matrix theory (28), the reflection coefficient of the matrix, $\sigma = (1-\phi)^2$, where, the partition coefficient ϕ is given as $\phi = 1 - V_f(1 + a/r_f)^2$. Here a is the molecular radius, r_f the fiber radius, and V_f the fiber volume fraction. For the hexagonal fiber array shown in Fig. 1B, $V_f = 2\pi r_f^2/\sqrt{3}(2r_f + \Delta)^2$ where Δ is the fiber gap. For $a = 3.5$ nm (albumin), $r_f = 6$ nm, and $\Delta = 8$ nm, $\sigma = 0.67$. In contrast, if $r_f = 0.6$ nm and $\Delta = 8$ nm, values typical of the extended glycosaminoglycan fiber array, $\sigma = 0.52$. Because the measured value of σ is typically >0.8 (29), the structural model proposed in ref. 15 provides better agreement than a model based on extended GAG sidechains. Similar results for a square fiber array are presented in ref. 15. These predictions underestimate σ , because albumin is an ellipsoidal and not a spherical molecule, and the negatively charged arginine groups on the albumin molecule will interact with the negative charge on the molecular filaments of the glycocalyx (30).

A more stringent test of the ultrastructural model for the ESL proposed in ref. 15 is the relative contribution of the ESL to the total hydraulic resistance of the endothelial layer in the calculation of the filtration coefficient L_p . The model sketched in Fig. 2A has provided reasonable predictions for the solute permeability data for most solutes up to the size of albumin using an ESL comprised of extended GAG side chains with $r_f = 0.6$ nm and $\Delta = 7-8$ nm (5). However, the model cannot explain the doubling of L_p observed in ref. 31 for frog mesentery microvessels when the ESL is removed after pronase treatment. The model in ref. 5 predicts the measured L_p of 2.0×10^{-7} cm \cdot s $^{-1}$ /cmH $_2$ O (1 cmH $_2$ O = 98 Pa) for junction breaks $2d = 150$ nm in length, spaced every $2D = 2,640$ nm if the fiber layer thickness, L_f , is 150 nm, a value consistent with the electron microscopic observations in ref. 15 and 19. However, L_p increases only to 2.3×10^{-7} cm \cdot s $^{-1}$ /cmH $_2$ O, or $\approx 15\%$, when the ESL is removed if the surface layer consists of extended GAG sidechains. The hydraulic resistance of the ESL is far too small to account for the measured doubling in L_p when it is removed.

These calculations have been repeated for the new model for the ESL proposed in ref. 15, namely a hexagonally ordered matrix with much larger core protein fibers of effective radius $r_f = 6$ nm, $\Delta = 8$ nm, and $L_f = 150$ nm. One finds that an L_p of 2.0×10^{-7} cm \cdot s $^{-1}$ /cmH $_2$ O is achieved for control conditions when the orifice spacing $2D$ is reduced to 2,025 nm. The solution for the pressure distribution just behind the surface layer, $x = 0$, and just in front and behind the TJ strand, $x = 200 \pm$ nm, is shown in Fig. 2B. One notes that the pressure at the orifice break is nearly uniform and has a value 4.2 cmH $_2$ O when the lumen pressure is 15 cmH $_2$ O. If the glycocalyx is removed, the pressure at the break would increase to 7.5 cmH $_2$ O. Because the flow across the endothelial layer is proportional to the difference in pressure between the orifice and the cleft exit, where the hydraulic pressure is assumed to be zero, the predicted value of L_p increases to 3.6×10^{-7} cm \cdot s $^{-1}$ /cmH $_2$ O when the glycocalyx is removed. A doubling of L_p would be achieved if L_f is 200 nm. The proposed new structure in Fig. 1 provides a much improved description of the hydraulic resistance of the ESL as well as a better prediction for σ .

Hydrodynamic Forces and Torques. We next describe an idealized mathematical model to predict the forces and bending moments acting on the vertical filaments (core proteins) of the bush-like structures comprising the ESL. These filaments, when observed *en face*, are assumed to form a hexagonal array as depicted in Fig. 1B. The basic model closely parallels the hydrodynamic model developed in ref. 32 for determining the forces and bending moments acting on the brush border microvilli in the proximal tubule, where transverse sections show that the microvilli form a highly ordered hexagonal array. In ref. 32, the forces and

bending moments on the microvilli are used to explore a new mechanosensory hypothesis to explain the afferent mechanism in “glomerulotubular balance.” In the present application, we consider a capillary of circular cross section of radius R_o in which filaments of uniform length L_f protrude radially into the interior of the vessel. Effective medium theory (Brinkman equation),

$$\frac{\partial p}{\partial z} = \frac{\mu}{R} \frac{\partial}{\partial R} \left(R \frac{\partial U}{\partial R} \right) - \frac{\mu}{K_P} U, \quad [1]$$

is used to describe the flow in the wall layer (7, 13, 33, 34). Here K_P is the Darcy permeability of the ESL, and μ is the plasma viscosity. Outside the wall layer, one has a classical unidirectional viscous flow with a Poiseuille profile.

Following the approach in ref. 32, we determine the Darcy permeability K_P by using the solutions in ref. 34 for the local 2D Stokes flow past a hexagonal array of circular cylinders. An approximate expression for the relationship between K_P/r_f^2 and the fiber volume fraction, $c = 2\pi r_f^2/\sqrt{3}(2r_f + \Delta)^2$, is

$$\frac{K_P}{r_f^2} = \frac{\ln(c^{-1/2}) - 0.745 + c - c^2/4}{4c}. \quad [2]$$

Eq. 2 is valid for $c < 0.4$. One can define a periodic unit for the hexagonal fiber array and derive a simple expression for the local drag force per unit fiber length $F(R)$ acting on each vertical fiber (32). This local expression for the drag is

$$F(R) = \frac{\pi \mu U(R)}{c} \frac{r_f^2}{K_P}, \quad [3]$$

where $U(R)$ is the local average velocity for the flow past the fiber obtained from the solution of Eq. 1 in the ESL. One finds that for $r_f = 6$ nm, $\Delta = 8$ nm, and $L_f = 150$ nm, the slip velocity U at the outer edge of the ESL is only 3 μ m/s when the shear stress at the edge of this layer is 10 dyn/cm 2 . This is only 0.2% of the centerline velocity of 1.4 mm/s in a 5- μ m-diameter capillary at this shear stress. Deeper within the matrix layer, the velocity decays to a nearly uniform value of only 6 nm/s (0.2% of the edge velocity). This slow uniform flow is driven by the axial pressure gradient in the capillary. Thus, the shear stress on the membrane is negligible. The fluid shear force acting on the edge of the matrix layer is converted in the ESL to a drag force that acts on the tips of the core proteins that extend through the layer. This model assumes that the deformation of the ESL can be neglected in solving Eq. 1 for $U(R)$.

If the local drag $F(R)$ in Eq. 3 is integrated from the tip of the core protein, one finds that 90% of the total drag, 4.4×10^{-4} pN, arises from the flow in a tip interaction layer that lies within 25 nm of the edge of the ESL when $L_f = 150$ nm, and the shear stress at the outer edge of the ESL is 10 dyn/cm 2 . Using this drag distribution, one can show that 96% of the total bending moment, 0.061 pN \cdot nm, arises from the flow in this tip interaction layer. For $L_f = 400$ nm, the ESL thickness in hamster cremaster (2), the total drag is 7.0×10^{-4} pN, and the bending moment 0.23 pN \cdot nm. These predictions for the drag and bending moment scale linearly with the shear stress.

Flexural Rigidity EI of Vertical Fibers. The key parameter in determining how the core proteins transmit hydrodynamic and mechanical forces across the ESL is their bending rigidity EI . In ref. 8, the bending rigidity of the fibers is neglected, and the structural rigidity of the layer is attributed to a weak colloidal osmotic pressure that resists the normal component of the tension imposed by the fluid shearing stress. Detailed solutions in ref. 6 for the protein concentration distribution across the ESL show there is a sharp drop in concentration across the ESL even in the presence of back loading of the tissue. Thus, the oncotic

pressure in the plasma should be significantly greater and not less than in the ESL. This would appear to negate the possibility that an oncotic pressure provides for the structural rigidity of the surface layer.

In this study, we propose an alternate hypothesis, namely that the core proteins have a finite bending rigidity sufficient to withstand the bending moments created by the drag forces on their tips in the fiber interaction layer. Three observations strongly support this hypothesis. First, it is hard to explain how the glycocalyx could maintain its periodic structure in the presence of thermal fluctuations due to Brownian motion were it not for a significant bending rigidity of the core proteins. Second, the molecular sieving properties of the glycocalyx described in the section on transport cannot be explained by slender highly flexible GAG sidechains but are consistent with a more rigid molecular structure associated with the core proteins. Third, the *in vivo* measurements (2) for L_f and the fluid gap between the edge of the surface layer and the red cell membrane indicate little or no deformation of the ESL occurs for red cell velocities $>20 \mu\text{m/s}$.

There are, to our knowledge, no direct measurements of EI for the core proteins of proteoglycans equivalent to the studies that have been performed for F-actin, collagen fibrils, and microtubules (35–37). Therefore, we have developed an indirect approach for estimating EI . Vink and Duling (2) observed that the ESL could be substantially compressed by either the passage of a WBC or the arrest of motion of a red cell. To quantify this effect and determine the time-dependent recovery of the ESL, Vink *et al.*⁸ measured the gap between the endothelial and red cell membranes of red cells that passed in the wake of the WBC. By measuring the time lag between the passage of the red cell and WBC, one could measure the time-dependent restoration of this gap. Because the fluid space between the outer edge of the compressed ESL and the red cell did not noticeably change, most of the change in displacement of the red cell membrane from the endothelial surface could be attributed to the change in thickness of the ESL. The recovery curve for the displacement of the red cell can be approximately described by a single exponential with a characteristic time of 0.38 s. We shall determine EI by constructing an approximate viscoelastic model for this recovery.

We assume that the roots of each bush-like cluster in Fig. 1 are firmly anchored by short linker molecules into the underlying CC (24). Thus, each vertical filament can be modeled as a cantilever beam, whose initial loading due to the passage of the WBC is modeled by a horizontal force P applied at the tip of the deforming core protein. The energy stored in elastic deformation of the core proteins will be expended in the viscous dissipation of the recoiling fibers. The local drag on the fibers is proportional to the local instantaneous velocity of the fiber relative to the fluid motion. However, our previous solutions show that the fluid trapped in the glycocalyx is nearly stagnant except for a thin tip interaction layer, which we shall neglect. Thus, the local expression for the force on the fiber per unit length is from Eq. 3 given by $F = (\pi\mu U/c)r_f^2/K_P$, where $U(x, t)$ is now the instantaneous local fiber velocity, and K_P , given by Eq. 2, describes the hydrodynamic interaction between fibers. If $y(x, t)$ is the local deflection of the fiber, then $U = \partial y/\partial t$. For small deflections, the viscoelastic recoil of the fiber is given by

$$EI \frac{\partial^4 y}{\partial x^4} = -\frac{\pi \mu r_f^2}{c K_P} \frac{\partial y}{\partial t} \quad [4]$$

In solving Eq. 4, we neglect the time-dependent changes in K_P as the glycocalyx expands and nonlinear effects of large deformation. Because the final phase of the recoil is described by the long time mode for the fiber recovery and not the rapid initial phase of large deformation, Eq. 4 should provide a reasonable lowest-order approximation for the recovery time.

Eq. 4 can be cast in dimensionless form by introducing the dimensionless coordinates $X = x/L$ and $Y = y/y(L, 0)$. Here L is the length of the core protein, and $y(L, 0) = PL^3/(3EI)$ is the initial tip deflection for an initial load P applied at $x = L$. We draw a distinction between L and the ESL thickness, L_f , because below we will consider large changes in L_f in which L is unchanged. The dimensionless time T is given by $T = t/\tau$, where $\tau = kL^4/EI$ and $k = (\pi/c)(\mu r_f^2/L_P)$ are the coefficient of the velocity term in Eq. 4. We wish to solve the dimensionless form of Eq. 4, $Y_{XXXX} = -Y_T$, subject to the dimensionless boundary and initial conditions:

$$Y(0, T) = \frac{\partial Y(0, T)}{\partial X} = \frac{\partial^2 Y(1, T)}{\partial X^2} = \frac{\partial^3 Y(1, T)}{\partial X^3} = 0, \quad [5 \text{ a, b, c, d}]$$

$$Y(X, 0) = \frac{3}{2}X^2 - \frac{1}{2}X^3. \quad [5e]$$

The initial condition Eq. 5e is the quasisteady shape of a cantilever beam subject to a concentrated transverse load P at its end.

The solution of the boundary value problem defined by Eqs. 4 and 5 is not straightforward, and we briefly summarize the solution procedure. The viscous loading term on the right-hand side of Eq. 4 is first expressed in an infinite series of the form

$$-\frac{\partial Y}{\partial T} = a_2 X^2 + a_3 X^3 + a_4 X^4 + a_5 X^5 + \dots, \quad [6]$$

where the $a_i(T)$, $i = 2, 3, 4 \dots$ are unknown time-dependent functions. The form of Eq. 6 is dictated by the initial deformed shape of the fiber, Eq. 5e. When the latter series is substituted into Eq. 4, integrated term by term, and the first two boundary conditions (Eq. 5 a and b) applied, one finds that all of the $a_i(T)$ can be expressed in terms of just two unknown functions of time $f_2(T)$ and $f_3(T)$ that arise from the integration of Eq. 4. The solution for $Y(X, T)$ takes the form

$$Y = f_2 \cdot \frac{X^2}{2} + f_3 \cdot \frac{X^3}{6} - f_2' \cdot \frac{X^6}{720} - f_3' \cdot \frac{X^7}{5040} + f_2'' \cdot \frac{X^{10}}{5040 \times 720} + f_3'' \cdot \frac{X^{11}}{5040 \times 7920} + \dots \quad [7]$$

One notes that the series solution, Eq. 7, is rapidly convergent. Because the terms in X^{10} and X^{11} involve inertia and the latter is very small in a viscous-dominated flow, the series solution, Eq. 7, has been truncated at X^7 . Application of boundary conditions Eq. 5 c and d leads to a coupled set of differential equations for $f_2(T)$ and $f_3(T)$ that must satisfy initial condition Eq. 5e. The solution of this initial value problem leads to lengthy expressions containing two exponentials, one $e^{-T/0.0044}$ and the other $e^{-T/0.0789}$. The first describes the early time decay of the initial profile described by Eq. 5e and the second, the longer time decay of the fundamental mode. The details of the complete solution can be found in *Appendix A*, which is published as supporting information on the PNAS web site, www.pnas.org.

It is the long time decay that we wish to match with the exponential describing the time-dependent restoration of the ESL in Vink *et al.*⁸ This is done by setting $0.0789\tau = \beta$ s, where $\beta = 0.38$ is the exponential fit to the experimental recovery curve in Vink *et al.*⁸ From the definition of τ and k

$$EI = \frac{0.0789}{\beta} \frac{\pi \mu r_f^2}{c K_P} L^4. \quad [8]$$

For $\beta = 0.38$, $r_f = 6$ nm, $\Delta = 8$ nm, and $L = 0.4 \mu\text{m}$, $c = 0.326$, $K_P = 3.157 \text{ nm}^2$, and $EI = 700 \text{ pN}\cdot\text{nm}^2$. In comparison, the

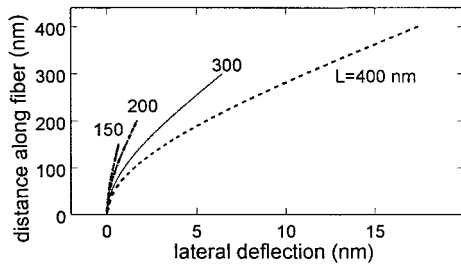


Fig. 3. Model predictions for lateral deflection of core proteins of different lengths L for a fluid shear stress of 10 dyn/cm^2 at ESL edge. $EI = 700 \text{ pN}\cdot\text{nm}^2$.

measured values of EI for an actin filament vary between $15 \times 10^3 \text{ pN}\cdot\text{nm}^2$ (36) and $73 \times 10^3 \text{ pN}\cdot\text{nm}^2$ (37). One observes that EI for an actin filament is at least 21-fold greater than the core proteins. Thus, if the core proteins are anchored into the CC through a transmembrane protein complex, as sketched in Fig. 1, this supporting structure will be much stiffer than the core proteins in the ESL, justifying our use of a cantilever beam model in solving Eq. 4.

Deformation of Core Proteins Due to Fluid Shear. The hydrodynamic loading on the core proteins given by Eq. 3 can be used to predict their deformation when subject to fluid shear. Following the analysis described in ref. 32, one can split the total loading into two contributions, a concentrated load P applied at $x = L$, due to the fluid drag associated with the tip interaction layer, and a uniformly distributed load q associated with the much slower pressure-driven flow in the interior of the ESL. One obtains the following simple expression for the shape of the fiber, using classical beam theory,

$$y(x) = \frac{1}{EI} \left[\frac{P}{6} (-x^3 + 3Lx^2) + \frac{q}{24} (x^4 - 4Lx^3 + 6L^2x^2) \right]. \quad [9]$$

Eq. 9 has been plotted in Fig. 3 for fibers ranging in length from 150 nm, the ESL thickness observed in ref. 15 for frog mesentery capillary, to 400 nm, the thickness of the excluded fluorescent dextran layers observed in ref. 2 for hamster cremaster. Results are shown for a fluid shear stress of 10 dyn/cm^2 at the edge of the ESL and a bending rigidity $EI = 700 \text{ pN}\cdot\text{nm}^2$. The tip deflection of the longest fiber is only 17.9 nm. Thus, all deflections are well within the limits of small deflection theory. The important conclusion is that the fibers have sufficient flexural rigidity to resist bending at fluid shear stresses in the physiological range and, as observed in refs. 2 and 16, there is no observable deformation of the ESL due to fluid shear. The structural integrity of the glycocalyx can be maintained without the need for oncotic swelling forces (14) or electrochemical hydration resulting from distributed negative charge on extended GAG sidechains (30).

Deformation Due to Red Cell Motion. One of the striking observations in ref. 2 is that when the red cell motion is arrested, the cell expands to fill nearly the entire capillary lumen. At very low velocities, $<20 \mu\text{m/s}$, the red cell membrane slowly lifts off the wall and, at velocities $>20 \mu\text{m/s}$, the cell “pops out” of the layer and glides above the glycocalyx with a fluid gap that increases nearly linearly with increasing speed as observed in figure 3 of ref. 2. The “pop-out” behavior while the cell is still in the ESL has been examined in refs. 7 and 8. In ref. 7, it is shown that the compression of the layer is closely akin to snowboarding on fresh snow powder. The fluid is trapped within the fibers of the compressed matrix and is unable to fully escape on the time scale of the cell passage, with the result that lubrication pressures far greater than predicted by

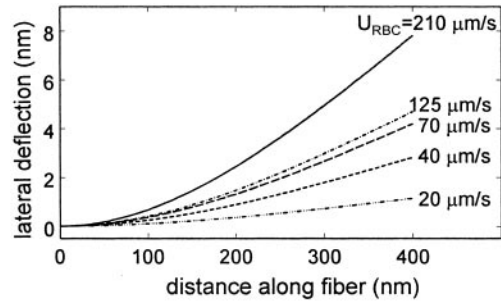


Fig. 4. Model predictions for lateral deflection of core proteins beneath red cells moving at different velocities U_{RBC} . Spacing δ between ESL edge and red cell taken from measurements in ref. 2.

classical lubrication theory can be generated. The analysis in ref. 8 considers a deformable cell whose membrane is subject to fluid shear and bending deformation. The latter analysis provides intuitive insight into the shape changes that occur for an axisymmetric cell during lift off from the capillary wall. Neither Feng and Weinbaum (7) nor Secomb *et al.* (8) consider the viscoelastic deformation of the ESL.

We first develop a simple model for the deformation of the ESL when the red cell is gliding above its outer edge at velocities $>20 \mu\text{m/s}$. The observations in ref. 2 show a nearly uniform fluid gap δ between the outer edge of the ESL and the red cell membrane that increases initially with increasing velocity and then asymptotes to a nearly uniform gap. This suggests a simple 2D model for the fluid motion in the confined region, a parallel channel flow with two layers, a Brinkman layer (Eq. 1 written in x, y coordinates) of thickness L_f on the bottom to describe the ESL and a clear plasma layer of thickness δ on top. At the interface between the regions, one requires that the average velocity have a discontinuity to take account of the solid fraction of the matrix. Similarly, there is a discontinuity in the average fluid shear stress. Using Eq. 2, one first obtains closed-form solutions for the velocity field across the ESL, providing analytic expressions for the hydrodynamic loading $F(y)$ in the beam equation for the deflection of the core proteins as described previously when the red cell was not present.

The results of the above model have been plotted in Fig. 4 by using the same parameter values for the ESL as used in Fig. 3. The novel feature of this solution is that the increase in the fluid gap δ as a function of the red cell velocity U_{RBC} has been estimated by using the measured data in figure 3 of ref. 2. This allows us to circumvent the much more difficult problem of developing a model for finding the change in red cell shape as a function of its velocity and capillary diameter when our primary interest is the forces and bending moments on the vertical fibers and their deformation. Fig. 4 shows our predictions for the change in fiber shape as a function of increasing red cell velocity from 20 to $210 \mu\text{m/sec}$ for red cells traveling in a $5\text{-}\mu\text{m}$ -diameter hamster cremaster capillary where L_f is $0.4 \mu\text{m}$. One observes that the magnitude of the tip deflection at $210 \mu\text{m/s}$ is about one-half that shown in Fig. 3 for a shear stress of 10 dyn/cm^2 but decreases rapidly as the red cell velocity and fluid gap δ decrease.

ESL Deformation Due to Red Cell Arrest. One would like to know the maximum pressure that the ESL can withstand without its fibers buckling when the red cell comes to rest. One would also like to compare this pressure with the fluid pressure generated in draining the fluid trapped in the matrix between the red cell and EC membranes. A simplified model will be developed for estimating the latter pressure.

The governing equation for the bending of a curved beam

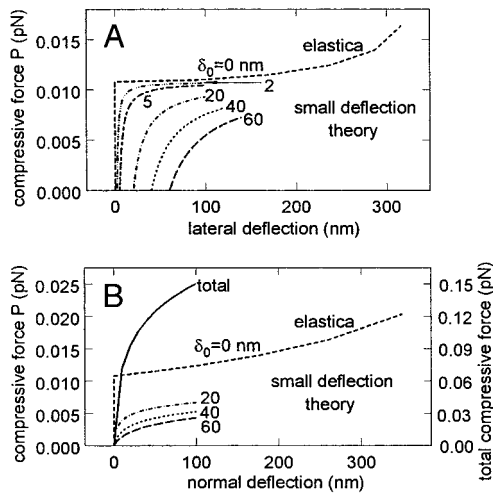


Fig. 5. (A) Predictions of Eq. 12 for lateral tip deflection due to buckling of core proteins subject to a normal load P applied at their ends. δ_0 is the initial unloaded tip displacement from vertical shown in Fig. 1B. Curve for $\delta_0 = 0$ is “elastica” theory prediction for large deflections (38). (B) Results in A converted to normal displacement of ESL. Right ordinate is the compressive force for 27-fiber model for core protein cluster in Fig. 1B.

whose initial shape is given by a curve $y_0(x)$ subject to a compressive force P acting at its end is

$$EI \frac{d^2(y - y_0)}{dx^2} = P(\delta - y), \quad [10]$$

where δ is the unknown tip deflection after the load P is applied. A simple parametric description of the initial shape of the fibers in Fig. 1A is $y_0(x) = \delta_0 \sin(\alpha x)$, where $\alpha = \pi/2L_f$, and δ_0 is the initial tip deflection. The solution of Eq. 10 that satisfies the boundary conditions $y(0) = 0$ and $y'(0) = \delta_0 \alpha$ is

$$y(x) = \delta - \delta \cos(kx) + \frac{\delta_0 \alpha k}{k^2 - \alpha^2} \sin(kx) - \frac{\delta_0 \alpha^2}{k^2 - \alpha^2} \sin(\alpha x), \quad [11]$$

where $k = \sqrt{P/EI}$. If we now require that $y(L) = \delta$ in Eq. 11, then the unknown tip deflection is given by

$$\delta = \frac{\delta_0 \alpha}{k^2 - \alpha^2} \frac{k \sin(kL) - \alpha \sin(\alpha L)}{\cos(kL)}. \quad [12]$$

The tip deflection given by Eq. 12 is plotted in Fig. 5A for the case where $L = 0.4 \mu\text{m}$ and $EI = 700 \text{ pN}\cdot\text{nm}^2$. The critical load for the buckling of a straight fiber using small deflection theory is $P_{cr} = \alpha^2 EI$. For the foregoing values of L and EI , $P_{cr} = 0.0108 \text{ pN}$. Elastica theory (38) for large deformations must be used to determine the displacement for this critical load, because small incremental loads above P_{cr} will cause large deflections. This result using elastica theory is given by the uppermost curve in Fig. 5A. One observes that fibers that are initially not straight will support compressive loads far smaller than P_{cr} . Returning to Fig. 1B, one observes that on average 27 core proteins terminate in each cluster foci, taking into account shared proteins at hexagonal cluster boundaries. Surrounding each central core protein there are six core proteins in the first hexagon, 12 in the second hexagon, and 18 in the outer border hexagon, 12 of which are shared by two clusters and six of which are shared by three clusters. The maximum compressive force that could be supported by each bush-like structure is $\approx 0.3 \text{ pN}$ if each fiber could support the critical load. However, most of the

fibers are either initially bent or loaded off axis, with the result that they carry a load far less than the critical load. For fibers that are initially bent, there is no critical load.

Using the results in Fig. 5A, one can construct a simple model to estimate the increase in normal force that would be exerted by each 27-fiber cluster if the ESL was subject to a uniform compression by a planar surface. One assumes that each fiber extends to the edge of the ESL during the compression, and the vertical displacement of each fiber is the same. The tip deflection δ in Eq. 12 is adjusted to satisfy this constraint, and the deformed shape of the fiber is given by Eq. 11. The downward (vertical) displacement of the fiber is determined by requiring that the initial fiber length L be conserved. To simplify the model for a fiber cluster, we assume that the fibers are arranged in three concentric circles rather than hexagons about the central core protein. The initial tip deflections are 20, 40, and 60 nm in each circle. The increase in normal force as a function of the downward displacement of a fiber in each of the three concentric circles is plotted in Fig. 5B. These results are shown for vertical deflections up to 100 nm, because Eqs. 11 and 12 are limited by the assumptions of small deflection theory. However, the curve for the central core protein is given by elastica theory for large deflections, and this result provides a useful upper bound. The right-hand ordinate in Fig. 5B provides the summation of the normal forces exerted by all 27 fibers in cluster foci. For a downward displacement of 100 nm, the compressive force on a cluster would be 0.15 pN or $\approx 1/2$ of the maximum compressive force of 0.3 pN cited earlier. Because the *en face* area of each cluster is $9.4 \times 10^3 \text{ nm}^2$, the resisting pressure of the fibers for this deflection is 160 dyn/cm^2 .

We would like to compare this elastic restoring force with the excess pore pressure created by the draining of the fluid from the ESL when the motion of a red cell is arrested. The latter is estimated by considering the stationary red cell as a cylindrical pellet of constant radius that uniformly expands under an applied pressure P_C to crush the glycocalyx. To simplify the model, we have neglected the deformation of the red cell membrane due to the fluid drainage, membrane elastic properties, and the initial stress-free configuration of the cell in its biconvex shape. These membrane-related considerations lead to complex shapes for the red cell membrane described in ref. 39 for a compressed red cell or in ref. 8 for a moving axisymmetric cell. The motion of the fluid in the glycocalyx satisfies Darcy’s law and continuity. The thin fiber interaction layers near the endothelial and red cell membranes are neglected. The flow in the layer is treated as a time-dependent flow in a compressible porous medium whose velocity varies as a function of time and distance from the leading or trailing edge of the pellet. We wish to capture the large-amplitude deformation of the ESL and the changes in K_P that result from this deformation. The change in K_P as a function of L_f is modeled by using the solutions in ref. 34 for the slow flow through a face centered periodic array of spheres whose solid fraction c changes as a function of L_f . For the large deformations considered in this application, where the fibers are crushed, the fluid resistance of the compacted matrix is better represented by the spherical particles on the core proteins as opposed to cylindrical fibers.

The results of the model for the fluid drainage are shown in Fig. 6. The time scale for the drainage is determined by the observation that the gap between the red and EC membranes nearly vanishes in 0.5 s. We assume that the expansion pressure P_C exerted by the spectrin CC of the red cell and its internal hydrostatic pressure are constant over the draining process, and the elastic restoring force of the glycocalyx is neglected. Two solutions for the time-dependent collapse of the glycocalyx are shown, one for a constant Darcy permeability K_P and a second for a time-varying decrease in K_P , where L_f is a function of c as described above. The details for both solutions can be found in

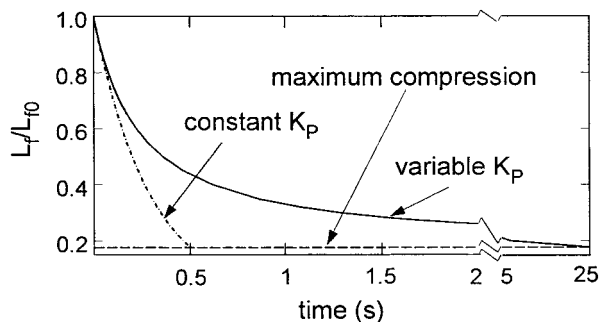


Fig. 6. Model prediction for time-dependent drainage of fluid from ESL after red cell arrest in a 5- μm -diameter capillary. A cell pressure of 2,420 dyn/cm^2 is required to fully collapse the layer within 0.5 s at constant K_P . This time is extended to 25 s if the variation of K_P with compression is considered.

Appendix B, which is published as supporting information on the PNAS web site. For constant K_P , the characteristic time is given by $\mu W^2/12P_cK_P$, where W is the pellet length. For the initial array $c = 0.13$, whereas for maximum compaction $c = 0.74$. For constant K_P , an applied pressure of 2,420 dyn/cm^2 is required to fully drain the ESL in 0.5 s. If this same pressure is applied in the variable K_P model, the total draining time is extended to 25 s. This applied pressure is 20 times the elastic buckling pressure of the core proteins in Fig. 5B, which justifies the neglect of the elastic restoring force in the fluid draining model.

Discussion

Collectively, the models presented herein have provided a view of the viscoelastic behavior of the ESL and its response to fluid shear and cellular motion or arrest. We will discuss the implications of these models for transport, fluid shear, red and white cell motion, and mechanotransduction, in that order.

Transport. Heretofore, the molecular sieving structure of the matrix had been widely assumed to be associated with extended GAG side chains periodically arranged along the core proteins of proteoglycans (5, 25, 28). These extended fibers were thought to be sialic acid side chains with typically 0.6-nm radius with a solid fraction c between 1% and 2% (15, 29). Because the structure of the proteoglycans was largely deduced from their 2D appearance when splayed out on carbon filters (27), it was never clear how the fibers formed a 3D lattice. It was assumed that in their extended state, the protein monomers had a bottle-brush appearance. The new structural model proposed in ref. 15 and quantitatively examined herein is a much denser and stiffer structure. The c of the 12-nm diameter scattering centers, which are assumed to be either aggregated GAG or attached proteins, is 0.13 for the hexagonal lattice in Fig. 1B, which does not even include the core protein backbone.

The structural model depicted in Fig. 1 is an appealing alternative in that it provides a reasonable 3D organization of the matrix consistent with the latest ultrastructural studies (15, 20) and yields improved quantitative predictions for both σ and L_p . The hexagonal fiber arrangement in Fig. 1B yields a somewhat better fit to the experimental data for σ than the square fiber array in ref. 15. The model for L_p in Fig. 2 is able to explain the 2-fold increase in L_p in frog mesentery capillary when the glycocalyx is enzymatically removed by pronase digestion (31). This prediction, although satisfying, is not conclusive in that proteases are nonspecific enzymes whose effect on TJ structure has not been quantified. However, the electron microscopic studies performed in ref. 31 show a nearly complete fragmentation and removal of the ESL and no obvious changes in the TJs.

Bending Rigidity. An important prediction of this study is the bending stiffness of the core proteins in the bush-like clusters that decorate the endothelial surface. The value of EI , 700 $\text{pN}\cdot\text{nm}^2$, predicted by our model for the restoration of the ESL after the passage of a WBC, is at least 20 times less than the measured EI for actin filaments (36, 37) but sufficiently stiff to resist large deformations of the ESL due to fluid shear stresses in the physiological range. The tip deflections predicted for a shear stress of 20 dyn/cm^2 in small arterioles would be twice those shown in Fig. 3 or ≈ 35 nm for a fiber of 400-nm length. The much larger value of EI for the actin filaments in the underlying CC indicates that the CC provides a firm support for the short linker molecules that attach the transmembrane proteins at the base of each bush-like cluster to the submembrane scaffold. We propose that it is these root-like connections that firmly anchor the fiber clusters.

Red Cells. Because red cells are continuously flowing through our capillary beds with an intermittency that causes their velocity to vary widely, one would intuitively expect that their motion does not cause frequent disruptive interactions with the ESL. The predicted structural properties of the core proteins appear to be finely attuned to this motion. Fig. 4 shows that the passage of red cells over a wide range of velocities from 20 to >200 $\mu\text{m}/\text{s}$ causes only minor deformations of the core proteins. At velocities <20 $\mu\text{m}/\text{s}$, the observations in ref. 2 and the theoretical models (7, 8) predict that the red cell will enter the ESL. This will occur when the flow in a capillary is temporarily arrested by the passage of a red cell through a tightly fitting arteriolar sphincter at the entrance to a microvessel. Much larger repulsive forces are required here to prevent adhesive interactions between proteins in the red and EC membranes. The stiffness of the core proteins, although adequate to resist the penetration of red cells during their normal motion, is insufficient to prevent their buckling when red cell motion is arrested. Our model predicts that the buckling pressure for a core protein cluster is ≈ 100 pN/cm^2 when $L_f = 400$ nm and increases as $1/L_f^2$. The added resistance to the collapse of the glycocalyx arises from the time-dependent draining of the fluid in the compressed ESL. Our simplified model for the draining of this layer predicts that the pressure generated by the draining of the fluid trapped in the ESL is at least 20 times greater than the elastic restoring forces exerted by the core proteins in Fig. 5. It is this pressure and not the elastic response of the matrix that prevents the red cell from rapidly entering the matrix when its motion is arrested.

The characteristic fluid draining time for the ESL, $\mu W^2/(12P_cK_P)$, is a sensitive function of K_P . The results in Fig. 6 show that the draining time for large compressions is greatly extended by the large decrease in K_P that accompanies matrix compaction. This can be thought of as an additional safety factor preventing the adhesive interaction between proteins in the opposing membranes when motion is nearly arrested, allowing red cells to pass through constrained arterioles into capillaries without the flow coming to a stop. With few exceptions, red cells enter capillaries edge on and fold up on themselves much like a crepe. Their bending stiffness in this configuration is much greater than the axisymmetric configuration treated in ref. 8. In the latter study, the authors showed that an oncotic pressure of only 40 dyn/cm^2 would prevent the ESL from collapsing, less than the elastic buckling pressures predicted in Fig. 5. The large increase in pressure that can be generated by the folded cell in tightly fitting capillaries is due to the small radius of curvature of its inner plasmalemma in the folded edge on configuration.

An observation that has generated much controversy is the large difference in L_f observed in frog mesentery, 150 nm (15), and hamster cremaster capillaries, 400 nm (2). The present analysis provides a plausible functional explanation for the difference in L_f . If the core proteins are shorter, their ability to

withstand buckling increases as L^{-2} . Frog red cells, unlike mammalian red cells, have nuclei and thus should be much stiffer. On the basis of our analysis in Fig. 5, the effective buckling pressure should increase by a factor of 7.1 when L_f decreases from 400 to 150 nm. This increase in buckling pressure could compensate for the larger decrease in fluid draining time in the thinner ESL.

White Cells. In ref. 10, a model was developed to predict the contact forces that are generated when a WBC with protruding microvilli rolls on a planar surface in a gravitational field. It was shown that, due to lubrication layer effects, this lumpy roll can produce contact forces that are one to two orders of magnitude greater than the net sedimentation force of the WBC, which is ≈ 0.3 pN. For example, at wall shear stress of 10 dyn/cm², the normal contact force is 7 pN for 0.3- μ m microvilli of equal length, and that for a small population of longer 0.7- μ m microvilli, this contact force could increase to 27 pN. Because the diameter of the microvilli tips, ≈ 0.1 μ m, is approximately the same as each bush-like structure shown in Fig. 1B, and the elastic buckling force of the 27 core proteins in each structure is only of the order 0.1 pN, it is clear that the elastic properties of the ESL are insufficient to withstand the penetration of the microvilli tips. However, it is shown in ref. 40 that the major resistance to tip penetration arises from the viscous resistance of the ESL. The microvillus tip is modeled in ref. 40 as a sphere of 0.1- μ m diameter. This model is applied in ref. 10 to estimate the penetration depth of the microvilli if the matrix fibers were extended GAG side chains, where $r_f = 0.6$ nm and $\Delta = 8$ nm, as discussed earlier. For a wall shear stress of 10 dyn/cm², the predicted penetration depth was only 1 nm for equal-length microvilli and ≈ 20 nm for long microvilli of heterogeneous length. The short penetration depth is due to the very short microvillus tip contact times, which are < 0.1 ms at the above shear stress. Because the predicted K_p for the structural model in Fig. 1 is $\approx 1/3$ that for the extended GAG model, the predictions in ref. 10 for microvilli penetration are approximately a factor of three too large. A WBC can tip-toe across the ESL much like a Jesus Christ lizard can run across water (41). Tethered rolling in postcapillary venules is initiated by closely

fitting WBC whose microvilli tips are already in contact with the capillary endothelium when they first enter the venules (42).

Mechanotransduction. Single-particle tracking (22, 43) and optical traps (23, 24) have been used to probe the dimensions, 0.01–0.25 μ m², and the forces, 0.1–0.5 pN, required to deform the boundaries of the microdomains of the CC. The dimensions of the hexagonal actin network proposed in ref. 15 and sketched in Fig. 1B are at the lower end of this microdomain size. Studies using the gold-tagged transferrin receptor (TR) (24) have indicated that a force of 0.5 pN is required to drag the TR across microdomain boundaries, and that a smaller force of 0.1 pN will cause the boundary to undergo a large deformation with a measurable recoil when the particle is lost from the trap. The elastic constant for this recoil is 3×10^{-3} pN/nm (24). In this context, we note that the drag on a single core protein, 7.0×10^{-4} pN at a shear stress of 10 dyn/cm², is far too small to produce a significant deformation of the actin boundaries, but the entire bush-like core protein structure in Fig. 1 experiences a drag force of 1.9×10^{-2} pN, a force that would result in a 6-nm lateral displacement of an actin boundary. However, more revealing is the bending moment on the entire bush, 6.2 pN/nm. The long lever arm provided by the core proteins leads to a mechanical advantage that substantially amplifies the drag forces on the core protein tips when they are transmitted to the CC. A simple moment calculation applied to the actin network in Fig. 1B reveals that a vertical shear force of 0.05 pN would be experienced by the actin fibers, for a shear stress of 10 dyn/cm². This would correspond to an elastic recoil of 17 nm for a spring constant of 3×10^{-3} pN/nm. It is clear from this calculation that the mechanical advantage obtained by applying a small force at the tips of the core proteins provides sufficient leverage to deform the underlying CC. Our model predicts that, collectively but not individually, the core proteins in the bush-like structures in Fig. 1A are ideally suited to act as mechanotransducers that convert fluid shearing stresses at the edge of the ESL to deformations of the CC. We suggest that this is the initial activating step in intracellular signaling.

This research was supported by National Heart, Lung, and Blood Institute Grant HL-44485.

- Luft, J. H. (1966) *Fed. Proc.* **25**, 1773–1783.
- Vink, H. & Duling, B. R. (1996) *Circ. Res.* **79**, 581–589.
- Michel, C. C. (1997) *Exp. Physiol.* **82**, 1–30.
- Weinbaum, S. (1998) *Ann. Biomed. Eng.* **26**, 627–643.
- Hu, X. & Weinbaum, S. (1999) *Microvasc. Res.* **58**, 281–304.
- Hu, X., Adamson, R. H., Liu, B., Curry, F. E. & Weinbaum, S. (2000) *Am. J. Physiol. Heart Circ. Physiol.* **279**, H1724–H1736.
- Feng, J. & Weinbaum, S. (2000) *J. Fluid Mechanics* **422**, 281–317.
- Secomb, T. W., Hsu, R. & Pries, A. R. (2001) *Am. J. Physiol. Heart Circ. Physiol.* **281**, H629–H636.
- Damiano, E. R. (1998) *Microvasc. Res.* **55**, 77–91.
- Zhao, Y., Chien, S. & Weinbaum, S. (2001) *Biophys. J.* **80**, 1124–1140.
- Davies, P. F. (1995) *Physiol. Rev.* **75**, 519–560.
- Drenckhahn, D. & Ness, W. (1997) in *Vascular Endothelium: Physiology, Pathology, and Therapeutic Opportunities*, eds. Schwartz, C. J. & Born, G. V. R. (Schattauer, Stuttgart), pp. 1–25.
- Secomb, T. W., Hsu, R. & Pries, A. R. (1998) *Am. J. Physiol.* **274**, H1016–H1022.
- Secomb, T. W., Hsu, R. & Pries, A. R. (2001) *Biorheology* **38**, 143–150.
- Squire, J. M., Chew, M., Nneji, G., Neal, C., Barry, J. & Michel, C. C. (2001) *J. Struct. Biol.* **136**, 239–255.
- Henry, C. B. & Duling, B. R. (1999) *Am. J. Physiol.* **277**, H508–H514.
- Henry, C. B. & Duling, B. R. (2000) *Am. J. Physiol. Heart. Circ. Physiol.* **279**, H2815–H2823.
- Pries, A. R., Secomb, T. W. & Gaehtgens, P. (2000) *Pflügers Arch.* **440**, 653–666.
- Clough, G., Michel, C. C. & Phillips, M. E. (1988) *J. Physiol.* **395**, 99–114.
- Rostgaard, J. & Qvortrup, K. (1997) *Microvasc. Res.* **53**, 1–13.
- Michel, C. C. (1983) in *Pathogenicity of Cationic Proteins*, eds. Lambert, P. P., Bergmann, P. & Beauwens, R. (Raven, New York), pp. 125–140.
- Sako, Y. & Kusumi, A. (1994) *J. Cell. Biol.* **125**, 1251–1264.
- Edidin, M., Kuo, S. C. & Sheetz, M. P. (1991) *Science* **254**, 1379–1382.
- Sako, Y. & Kusumi, A. (1995) *J. Cell Biol.* **129**, 1559–1574.
- Fu, B. M., Weinbaum, S., Tsay, R. Y. & Curry, F. E. (1994) *J. Biomech. Eng.* **116**, 502–513.
- Adamson, R. H. & Michel, C. C. (1993) *J. Physiol.* **466**, 303–327.
- Buckwalter, J. A. & Rosenberg, L. C. (1982) *J. Biol. Chem.* **257**, 9830–9839.
- Curry, F. E. & Michel, C. C. (1980) *Microvasc. Res.* **20**, 96–99.
- Michel, C. C. & Curry, F. E. (1999) *Physiol. Rev.* **79**, 703–761.
- Damiano, E. R. & Stace, T. M. (2002) *Biophys. J.* **82**, 1153–1175.
- Adamson, R. H. (1990) *J. Physiol.* **428**, 1–13.
- Guo, P., Weinstein, A. M. & Weinbaum, S. (2000) *Am. J. Physiol. Renal. Physiol.* **279**, F698–F712.
- Sang, W. & Parker, K. H. (1995) *J. Fluid Mech.* **283**, 287–305.
- Sangani, A. S. & Acrivos, A. (1982) *Int. J. Multiphase Flow* **8**, 343–360.
- Kishino, A. & Yanagida, T. (1988) *Nature* **334**, 74–76.
- Dupuis, D. E., Guilford, W. H., Wu, J. & Warshaw, D. M. (1997) *J. Muscle Res. Cell Motil.* **18**, 17–30.
- Gittes, F., Mickey, B., Nettleton, J. & Howard, J. (1993) *J. Cell Biol.* **120**, 923–934.
- Timoshenko, S. P. & Gere, J. M. (1988) in *Large Deflections of Buckled Bars (the Elastica)* (McGraw-Hill, New York), pp. 76–82.
- Wu, R. & Weinbaum, S. (1982) *J. Fluid Mech.* **121**, 315–343.
- Feng, J., Ganatos, P. & Weinbaum, S. (1998) *J. Fluid Mech.* **375**, 265–296.
- Marks, B., Stowell, M. H., Vallis, Y., Mills, I. G., Gibson, A., Hopkins, C. R. & McMahon, H. T. (2001) *Nature* **410**, 231–235.
- Ley, K. (1996) *Cardiovasc. Res.* **32**, 733–742.
- De Brabander, M., Nuydens, R., Geuens, G., Moeremans, M. & De Mey, J. (1986) *Cell Motil. Cytoskeleton* **6**, 105–113.